Coupled-channel theory of photoionization microscopy

L. B. Zhao, I. I. Fabrikant, J. B. Delos, F. Lépine, S. Cohen, and C. Bordas

Phys. Rev. A **85**, 053421 — Published 25 May 2012

DOI: 10.1103/PhysRevA.85.053421

Coupled channel theory of photoionization microscopy

L. B. Zhao[†], I. I. Fabrikant[†,*], J. B. Delos[¶], F. Lépine[§], S. Cohen[‡], and C. Bordas[§]
[†] *Department of Physics and Astronomy, University of Nebraska, Lincoln, Nebraska 68588-0299, USA*
[*] *Department of Physical Sciences, The Open University, Walton Hall, Milton Keynes MK7 6AA, UK*
[¶] *Department of Physics, College of William & Mary, Williamsburg, Virginia 23187, USA*
[§] *Université Lyon I, LASIM, UMR CNRS n° 5579,*
43 Boulevard du 11 Novembre 1918, F69622 Villeurbanne Cedex, France and
[‡] *Atomic and Molecular Physics Laboratory, Physics Department, University of Ioannina, 45110 Ioannina, Greece*
(Dated: March 30, 2012)

We develop a quantum-mechanical coupled-channel theory to simulate spatial distributions of electron current densities, produced in photoionization for nonhydrogenic atoms in the presence of a uniform external electric field. The coupled Schrödinger equations are numerically solved using the renormalized Numerov method. The expression for the outgoing wave function for photoelectrons ejected from the nonhydrogenic atomic source has been derived. The theory is applied to investigations of photoionization for ground-state Li atoms. The distributions of electron current densities are computed and compared to the corresponding experimental images. Excellent agreement are obtained. It is furthermore found that the presence of the nonhydrogenic residual ion changes significantly the differential cross sections and/or electron current densities with respect to the hydrogenic case. Finally, the implications of the presence of the atomic core on quantum resonance tunneling are also analyzed.

PACS numbers: 03.65.Sq, 32.80.Fb, 07.81.+a

I. INTRODUCTION

Interference of outgoing electron waves produced in photoionization of atoms in the presence of a uniform external electric field was theoretically predicted in the 1980s[1,2]. The corresponding observation has been recently developed into an experimental technique, called photoionization microscopy[3–5], in which outgoing electron currents are measured using a velocity map imaging apparatus with a position-sensitive detector located at a macroscopic distance. This technique makes it possible to visualize electronic wave functions on a macroscopic scale, and therefore provides a means to get an insight into microscopic features of electronic motion near the nucleus. The electronic signals recorded at the detector form an image of a spatial interference pattern. The signal represented by the interference pattern is proportional to the square modulus of the electronic wave function, and carries information about the ionization process from small to large distances. During the last decade, substantial experimental and theoretical effort has been devoted to photoionization microscopy investigations.

The first experimental implementation of photoionization microscopy was made by Nicole *et al.*[4] following the pioneering work on slow photoelectron imaging[3]. Electrons ejected in photoionization of Xe from its metastable $6s[3/2]_2$ state were detected in a velocity map imaging apparatus. The obtained interference patterns were qualitatively explained within the framework of the semiclassical approximation, based on the calculation of the phase accumulated along classical electron trajectories. The structure of the interference pattern was found to evolve smoothly with the excess energy above the saddle point. The detailed semiclassical analysis and numerical simulations have been presented by Bordas *et al.*[6]. It was shown that the background contribution dominates in the Xe observations and the Stark resonances do not significantly affect the structure of the interference pattern.

The role of the Stark resonances in the interference pattern was investigated both in slow photoelectron imaging and in photoionization microscopy by the same group[7]. A number of them were clearly discerned in the Xe experiment. However, the various resonances observed were not assigned, because of the limitation of the semiclassical theory used in that paper. By means of the semiclassical analysis of the direct and indirect trajectories, Lépine *et al.*[7] concluded that some information regarding the localization of the wave function at a given Stark resonance may be inferred from the relative intensities of the direct and indirect ionization contributions in the image of low-kinetic-energy electrons.

More recently, Zhao and Delos[8] developed a semiclassical open-orbit theory for photoionization microscopy to describe the propagation of outgoing electron waves to macroscopic distances. The open-orbit theory provides a clear and intuitive physical picture through which the structures of spatial interference patterns observed in photoionization microscopy can be interpreted. It furthermore includes effects of Maslov indices, which may significantly alter the spatial distribution of the current densities, treats tunneling into classically forbidden regions, and corrects singularities at caustics and cylindrical foci by means of Airy-function and Bessel-function approximations. The open-orbit theory was applied to photoionization of hydrogenic atoms in an electric field, and the computed results are supported by the corresponding quantum-mechanical calculations[9].

The semiclassical open-orbit theory did not treat quantum resonance tunneling. A fully quantum-mechanical approach was developed by Zhao and Delos[9] to analyze the role of Stark resonances in the spatial interference patterns for the hydrogenic atom. They derived an expression of the outgoing wave function, and numerically solved the Schrödinger equation for both bound and continuous states using mixed semiparabolic and parabolic coordinates. The electron waves stemming from photoionization of hydrogen atoms from its $n = 2$ initial state in the presence of an electric field were propagated to large distances. The resulting probability densities were then compared to those from the open-orbit theory away from the resonances. Good agreement found between the results of the two treatments confirms the reliability of the semiclassical open-orbit theory.

The quantum-mechanical approach of Zhao and Delos[9] is valid only for hydrogenic atoms, but not for nonhydrogenic atoms. The pioneering theoretical work to simulate time-dependent electron currents produced in photoionization of nonhydrogenic atoms in a static electric field was performed by Robicheaux and Shaw[10], based on Harmin's approach[11,12]. The configuration space in this approach is divided into inner and outer regions, and the inner region is further divided into the core and Coulomb regions. In the inner region, the uniform electric field is negligible, and as a consequence, the photoabsorption process is adequately described by *field-free* parameters, quantum defects and dipole matrix elements of the relevant atoms in spherical coordinates. In the outer region, it is assumed that the electron moves in a Coulomb-Stark potential. This type of Hamiltonian is separable in parabolic coordinates. Following Harmin's idea, Robicheaux and Shaw[10] use the WKB approximation to evaluate the wave functions of outer electrons in a Coulomb-Stark potential, and the frame transformation matrix which connects wave functions in spherical and parabolic coordinates. Using the same method, Texier[13] calculated photoionization intensities for Xe atoms. In the present paper, we develop a fully quantum-mechanical theory, different from the WKB method of Robicheaux and Shaw[10], to simulate spatial distributions of electron currents and differential cross sections in photoionization microscopy experiments for nonhydrogenic atoms.

The paper is organized as follows. In Sec. II, the theory of the Stark effect in H atoms is reviewed. Section III is devoted to the development of the coupled-channel theory for nonhydrogenic atoms. We derive the expression for outgoing electron wave functions, produced by photoionization of nonhydrogenic atoms in a uniform electric field, and give details of numerical solutions of the coupled Schrödinger equations. Section IV describes a numerical method to locate resonances using the Bohr-Sommerfeld quantization condition for the purpose of comparison with those from the fully quantum-mechanical theory. This method is different from that of Ref.[8], where a solution of the classical Hamiltonian equations is required. In Sec. V, the developed coupled-channel theory is applied to Li atoms in electric fields, and the spatial distributions of electron current densities and differential cross sections are presented and compared to selected experimental results. Furthermore, the influence of the atomic core on distributions of electron current densities and differential cross sections is discussed in some detail. Section VI summarizes the coupled-channel theory of photoionization microscopy and our main conclusions. Atomic units are used throughout this paper unless otherwise noted.

II. THEORY OF THE STARK EFFECT IN HYDROGEN ATOMS

This section sketches theory of the Stark effect in H atoms and numerical solution procedures elaborated in Ref.[9], and gives main formulas relevant to the current derivation of the outgoing electron wave function.

The Schrödinger equation for the H atom in a uniform external electric field is separable in mixed semiparabolic and parabolic coordinates, $\xi = \sqrt{r+z}$, $\eta = r - z$, and $\phi = \tan^{-1}(y/x)$ (The reason to use semiparabolic rather than parabolic ξ coordinates was given in Ref.[9]). Let us denote the eigenfunctions of the Schrödinger equation as

$$\psi_{\epsilon n_1 m}(\xi, \eta, \phi) = \frac{u_\beta(\xi)}{\sqrt{\xi}} \frac{v_\beta(\eta)}{\sqrt{\eta}} \frac{e^{im\phi}}{\sqrt{2\pi}}, \tag{1}$$

where ϵ is the energy of the electron, n_1 is the node number of $u(\xi)$, m is the magnetic quantum number, and β is the separation constant. $u_\beta(\xi)$, $v_\beta(\eta)$ satisfy the ordinary differential equations

$$\left(\frac{d^2}{d\xi^2} + \frac{1 - 4m^2}{4\xi^2} - \mathscr{F}\xi^4 + 2\epsilon\xi^2 + 4\beta \right) u_\beta(\xi) = 0, \tag{2}$$

$$\left(\frac{d^2}{d\eta^2} + \frac{1 - m^2}{4\eta^2} + \frac{\mathscr{F}}{4}\eta + \frac{1 - \beta}{\eta} + \frac{\epsilon}{2} \right) v_\beta(\eta) = 0. \tag{3}$$

From these two equations, one readily sees that β is an implicit function of four parameters ϵ, $\mathscr{F}$, n_1, and m, namely $\beta(\epsilon, \mathscr{F}, n_1, m)$. Therefore, β represents the four indices, and to simplify notations, we will be writing β without

arguments. In some cases, β is replaced by n_1 as an index, when one implies that ϵ, $\mathscr{F}$, and m are fixed. The forms of Eqs. (2) and (3) show that the motion along the ξ coordinate is always bounded, while that along the η coordinate is oscillatory as $\eta \to \infty$. Thus $u(\xi)$ and $v(\eta)$ represent, respectively, the eigenfunctions for bound and continuum states.

The bound-state eigenvalue problem in Eq. (2) is numerically solved with the eigenvalue 2β. The one-dimensional ξ space is divided into two regions, the inner region and outer region. The inner region is a small vicinity near the nucleus, and the outer region is outside the small vicinity up to a sufficiently large value of ξ. In the inner region, $u(\xi)$ is expanded into a power series about the origin $\xi = 0$. In the outer region, outward integration of Eq. (2) is performed beginning from the boundary of the inner region and inward integration from a sufficiently large value of ξ using the renormalized Numerov method of Johnson[14]. The wave functions for the outward and inward integrations are matched at a suitable ξ point. For each given node number n_1 of the wave function $u(\xi)$, the eigenvalue 2β can be found by an iterative procedure. The obtained numerical solution $u(\xi)$ should satisfy the orthonormalization condition

$$\int_0^\infty u_{n_1}(\xi) u_{n_1'}(\xi) d\xi = \delta_{n_1 n_1'}. \tag{4}$$

Once the separation constant β is determined, the continuous-state eigenvalue problem in Eq. (3) may be numerically solved with the eigenvalue $\frac{1}{4}\epsilon$. Similarly, the one-dimensional η space is also divided into two regions. In a small vicinity near the nucleus, the eigenfunction $v(\eta)$ is expanded into a power series about the origin $\eta = 0$. Since the atomic states involved in the current problem are highly excited states and the wave function $v(\eta)$ of highly excited states oscillates rapidly, it is difficult to directly integrate Eq. (3). In the outer region, the Milne approach[15] is adopted to avoid the rapid oscillation of the wave function. Based on this approach, Eq. (3) is transformed into the nonlinear Milne equation. In this way, the oscillatory terms are extracted out, while the Milne function is very smooth and therefore there is no difficulty to solve the Milne equation. The renormalized Numerov method is a practical computational scheme. The outward integration of the Milne equation begins from the boundary between the inner and outer regions, while inner integration begins from a sufficiently large η value. Finally, the eigenfunctions are expressed as the Milne function $\mathcal{M}(\eta)$ times oscillatory terms,

$$v(\eta) = \mathcal{M}(\eta) \sin[\varphi(\eta) + \varphi_0], \tag{5}$$

$$\overline{v}(\eta) = \mathcal{M}(\eta) \cos[\varphi(\eta) + \varphi_0], \tag{6}$$

where $v(\eta)$ and $\overline{v}(\eta)$ represent the regular and irregular solution, respectively, with the asymptotic form at $\eta \to \infty$

$$v(\eta) \to \sqrt{\frac{2}{\pi k}} \sin[\varphi(\eta) + \varphi_0], \tag{7}$$

$$\overline{v}(\eta) \to \sqrt{\frac{2}{\pi k}} \cos[\varphi(\eta) + \varphi_0], \tag{8}$$

the phase $\varphi(\eta)$ is given by $\varphi(\eta) = \int \mathcal{M}^{-2}(\eta) d\eta$, and the initial phase φ_0 is determined by matching the wave functions from the outward and inward integration. In Eqs. (7) and (8), k refers to the wave number. The three-dimensional irregular parabolic eigenfunction is

$$\chi_{\epsilon n_1 m}(\xi, \eta, \phi) = \frac{u_\beta(\xi)}{\sqrt{\xi}} \frac{\overline{v}_\beta(\eta)}{\sqrt{\eta}} \frac{e^{im\phi}}{\sqrt{2\pi}}. \tag{9}$$

The orthonormalization relation of the parabolic eigenfunctions, and the Wronskian of $v(\eta)$ and $\overline{v}(\eta)$ can be proved to be as follows:

$$\left\langle \psi_{\epsilon' n_1' m'} \mid \psi_{\epsilon n_1 m} \right\rangle = \delta(\epsilon' - \varepsilon) \delta_{n_1' n_1} \delta_{m' m}, \tag{10}$$

$$W_\eta \left(v_\beta, \overline{v}_\beta \right) = 2/\pi. \tag{11}$$

III. COUPLED-CHANNEL THEORY

A. Solutions of the homogeneous Schrödinger equation

We formulate the standing-wave solutions, and incoming and outgoing parabolic solutions of the homogeneous Schrödinger equation in this section. The exact nonrelativistic Hamiltonian for N-electron atoms in an electric field directed along the z axis reads

$$\widehat{H} = -\frac{1}{2}\sum_{i=1}^{N}\nabla_i^2 - \sum_{i=1}^{N}\frac{Z}{r_i} + \sum_{i>j}\frac{1}{r_{ij}} + \sum_{i=1}^{N}\mathscr{F}z_i, \tag{12}$$

where Z is the atomic number. For alkali-metal atoms with a closed core and a valence electron in highly excited states, the complicated dynamics of the system may be substantially simplified to motion of the highly excited Rydberg electron in the Coulomb potential plus a short-range spherically-symmetric core potential. The corresponding Hamiltonian reads

$$\widehat{H} = -\frac{1}{2}\nabla^2 + V(r) + \mathscr{F}z, \tag{13}$$

with $V(r)$ satisfying boundary conditions $V(r) \overset{r\to 0}{\longrightarrow} -Z/r$ and $V(r) \overset{r\to\infty}{\longrightarrow} -1/r$. In mixed semiparabolic and parabolic coordinates, the Laplacian operator is written as

$$\nabla^2 = \frac{1}{\xi^2+\eta}\left[\frac{1}{\xi}\frac{\partial}{\partial\xi}\xi\frac{\partial}{\partial\xi} + 4\frac{\partial}{\partial\eta}\eta\frac{\partial}{\partial\eta}\right] + \frac{1}{\xi^2\eta}\frac{\partial^2}{\partial\phi^2}. \tag{14}$$

The Schrödinger equation for alkali-metal atoms in an electric field is

$$\frac{1}{\xi^2+\eta}\left[\frac{1}{\xi}\frac{\partial}{\partial\xi}\xi\frac{\partial\Psi}{\partial\xi} + 4\frac{\partial}{\partial\eta}\eta\frac{\partial\Psi}{\partial\eta}\right] + \frac{1}{\xi^2\eta}\frac{\partial^2\Psi}{\partial\phi^2} + 2\left[\epsilon - V(r) - \frac{1}{2}\mathscr{F}(\xi^2-\eta)\right]\Psi = 0. \tag{15}$$

Let us expand the wave function Ψ in functions $\Xi_{\beta'}(\xi) = u_{\beta'}(\xi)/\sqrt{\xi}$ and $\Phi(\phi) = \exp(im\phi)/\sqrt{2\pi}$ introduced in Eq. (1)

$$\Psi = \sum_{\beta'}\Xi_{\beta'}(\xi)\frac{1}{\sqrt{\eta}}F_{\beta'}(\eta)\Phi_m(\phi). \tag{16}$$

Substituting the above expression into Eq. (15) multiplied by $(\xi^2+\eta)/4$, one arrives, with the aid of Eq. (2), at

$$\sum_{\beta'}\left[\frac{\partial^2}{\partial\eta^2} + \frac{1}{2}\epsilon - \frac{m^2-1}{4\eta^2} + \frac{1}{4}\mathscr{F}\eta - \frac{\beta'}{\eta} - V(r)\frac{\xi^2+\eta}{2\eta}\right]u_{\beta'}(\xi)F_{\beta'}(\eta)\Phi_m(\phi) = 0. \tag{17}$$

Multiplication of this equation by $u^*_{\beta''}(\xi)\Phi^*_m(\phi)$ and integration over ξ, ϕ yield a set of coupled Schrödinger equations

$$\sum_{\beta'}\left[\widehat{h}_{\beta' m}\delta_{\beta''\beta'} - \mathcal{V}_{\beta''\beta'}(\eta)\right]F_{\beta'}(\eta) = 0 \tag{18}$$

with

$$\widehat{h}_{\beta' m} = \frac{d^2}{d\eta^2} + \frac{1}{2}\epsilon - \frac{m^2-1}{4\eta^2} + \frac{1}{4}\mathscr{F}\eta - \frac{\beta'}{\eta}, \tag{19}$$

$$\mathcal{V}_{\beta''\beta'}(\eta) = \left\langle u_{\beta''}(\xi)\left|V(r)\frac{\xi^2+\eta}{2\eta}\right|u_{\beta'}(\xi)\right\rangle. \tag{20}$$

It is obvious from Eq. (18) that the presence of the core couples parabolic channels, and each β value corresponds to one linearly independent solution that is a linear combination of channel wave functions. Therefore, it is essential

to add an additional subscript β to identify these solutions. The indexes β', β in $F_{\beta'\beta}$ identify *channel* and *solution*, respectively. Equation (16) is rewritten as

$$\Psi_{\epsilon\beta m} = \sum_{\beta'} \Xi_{\beta'}(\xi) \frac{1}{\sqrt{\eta}} F_{\beta'\beta}(\eta) \Phi_m(\phi). \tag{21}$$

To numerically solve the coupled Schrödinger equations (18), it is essential to explore the behavior of $F_{\beta'\beta}$ outside the core region. In the asymptotic region, $\eta \geq \eta_0$, $F_{\beta'\beta}$ has the form

$$F_{\beta'\beta} = v_{\beta'}\delta_{\beta'\beta} + \overline{v}_{\beta'}\mathcal{R}_{\beta'\beta}, \tag{22}$$

where $\mathcal{R}_{\beta'\beta}$ is the matrix element of the reaction matrix $\mathcal{R}$, and F represents the standing-wave solutions of the coupled Schrödinger equations (18). In compact matrix notation, Eq. (22) reads,

$$F = v + \overline{v}\mathcal{R}, \tag{23}$$

where v and $\overline{v}$ are diagonal matrix functions. Their diagonal elements are the regular and irregular parabolic solutions of Eq. (3) with the asymptotic forms given in Eqs. (7) and (8). It is convenient to utilize the matrix form of the standing-wave solutions to define the incoming and outgoing wave solutions $F^{\pm}$. Multiplying both sides of Eq. (23) by the matrices $\mp i(I \mp i\mathcal{R})^{-1}$, we obtain with the aid of Eqs. (7, 8)

$$F^{+} = -iF(I - i\mathcal{R})^{-1} = \frac{1}{2}\left(v^{-} - v^{+}\mathcal{S}\right), \tag{24}$$

$$F^{-} = iF(I + i\mathcal{R})^{-1} = \frac{1}{2}\left(v^{+} - v^{-}\mathcal{S}^{*}\right), \tag{25}$$

where I is the identity matrix, $\mathcal{S}^{*}$ indicates the complex conjugate of $\mathcal{S}$, $\mathcal{S}$ is the scattering matrix, given by

$$\mathcal{S} = (I + i\mathcal{R})(I - i\mathcal{R})^{-1}, \tag{26}$$

and $v^{\pm}$ are diagonal matrices with elements

$$v_{\beta}^{\pm} = \sqrt{\frac{2}{\pi k(\eta)}} e^{\pm i[\varphi_{\beta}(\eta) + \varphi_{0,\beta}]}. \tag{27}$$

The $\mathcal{S}$ matrix turns out to be unitary. If one replaces the standing-wave solution $F_{\beta'\beta}$ in Eq. (21) by $F^{-}_{\beta'\beta}$, the three-dimensional orthonormalized wave function is obtained

$$\Psi^{-}_{\epsilon\beta m} = \sum_{\beta'} \Xi_{\beta'}(\xi) \frac{1}{\sqrt{\eta}} F^{-}_{\beta'\beta}(\eta) \Phi_m(\phi). \tag{28}$$

In matrix notation, the equation reads

$$\Psi^{-} = i\Psi(I + i\mathcal{R})^{-1}, \tag{29}$$

where Ψ^{-} is a row matrix. The orthonormalization property of Ψ^{-} may be proved with the aid of Eqs. (10).

B. Outgoing wave functions with the atom-radiation field interaction

We begin from the inhomogeneous Schrödinger equation, namely an equation with a source describing the interaction between the atom and radiation field, to derive the expression for outgoing wave functions. The inhomogeneous Schrödinger equation reads

$$\left(\epsilon - \widehat{H}\right)\Psi(\mathbf{r}) = D\Psi_{ini}(\mathbf{r}) \tag{30}$$

where Ψ represents the wave function for the steady outgoing electron wave produced in photoionization in the presence of a uniform electric field pointing in the z direction, ϵ is the energy of the ionized electron, $D = \mathbf{e}\cdot\mathbf{r}$ is the dipole operator with $\mathbf{e}$ being the polarization vector, $\Psi_{ini}(\mathbf{r})$ is the atomic wave function for the initial state, and the

source term $D\Psi_{ini}(\mathbf{r})$ specifies the interaction between the atom and radiation field. Let us expand the solution of Eq. (30) in partial waves

$$\Psi(\mathbf{r}) = \sum_{\beta' m} \Xi_{\beta'}(\xi) \frac{\Lambda_{\beta'}(\eta)}{\sqrt{\eta}} \Phi_m(\phi). \tag{31}$$

Outside the core region, $\Lambda_{\beta'}$ should be proportional to $v^+_{\beta'}$, and therefore $\Psi(\mathbf{r})$ is written as a linear combination form of outgoing partial waves defined by Eq. (27),

$$\Psi(\mathbf{r}) = -i\frac{\pi}{2} \sum_{\beta' m} \mathcal{D}^-_{\beta' m} \Xi_{\beta'}(\xi) \frac{v^+_{\beta'}(\eta)}{\sqrt{\eta}} \Phi_m(\phi), \tag{32}$$

where the factor $-i\pi/2$ has been introduced for further convenience, the coefficients $\mathcal{D}^-_{\beta' m}$ should be such that the solution is regular at the origin. Following the method of Fink and Zoller[16], we will show now that these coefficients are reduced to the dipole matrix elements for transitions from the initial state to states $\Psi^-_{\epsilon\beta' m}$. Performing a derivation similar to that of Eq. (18), a set of coupled Schrödinger equations with source is generated. Multiplication of the resulting coupled equations from the left by $F^+_{\beta''\beta}(\eta)$ and summation over β'' give

$$\sum_{\beta''} \sum_{\beta'} F^+_{\beta''\beta}(\eta) \left[\widehat{h}_{\beta' m} \delta_{\beta''\beta'} - \mathcal{V}_{\beta''\beta'}(\eta) \right] \Lambda_{\beta'}(\eta) = \sum_{\beta''} \frac{F^+_{\beta''\beta}(\eta)}{\sqrt{\eta}} d_{\beta'' m}(\eta) \tag{33}$$

with

$$d_{\beta'' m}(\eta) = \int \Xi^*_{\beta''}(\xi) \phi^*_m(\phi) D\Psi_{ini} \frac{\xi(\xi^2+\eta)}{2} d\xi d\phi. \tag{34}$$

After replacing $F_{\beta'}(\eta)$ with $F^+_{\beta'\beta}(\eta)$ in Eq. (18), we manipulate the resulting equation in a same way to yield

$$\sum_{\beta''} \sum_{\beta'} \Lambda_{\beta''}(\eta) \left[\widehat{h}_{\beta' m} \delta_{\beta''\beta'} - \mathcal{V}_{\beta''\beta'}(\eta) \right] F^+_{\beta'\beta}(\eta) = 0. \tag{35}$$

The above equation remains unchanged if β'', β' are interchanged. Subtraction of Eqs. (33) and (35) gives

$$\sum_{\beta''} \left[F^+_{\beta''\beta}(\eta) \frac{d^2}{d\eta^2} \Lambda_{\beta''}(\eta) - \Lambda_{\beta''}(\eta) \frac{d^2}{d\eta^2} F^+_{\beta''\beta}(\eta) \right] = \sum_{\beta''} \frac{F^+_{\beta''\beta}(\eta)}{\sqrt{\eta}} d_{\beta'' m}(\eta). \tag{36}$$

After integration over η from 0 to $\overline{\eta}$, the equation becomes

$$\sum_{\beta''} W \left[F^+_{\beta''\beta}(\eta), \Lambda_{\beta''}(\eta) \right]_0^{\overline{\eta}} = \sum_{\beta''} \int_0^{\overline{\eta}} \frac{F^+_{\beta''\beta}(\eta)}{\sqrt{\eta}} d_{\beta'' m}(\eta) d\eta. \tag{37}$$

where $W(f_1, f_2)$ is the Wronskian of f_1 and f_2. Inserting Eqs. (24) and (32) into the equation, and noting that, since Λ_β is *regular* at the origin, $W\left[F^+_{\beta''\beta}(\eta), \Lambda_{\beta''}(\eta) \right]_{\eta=0} = 0$, we obtains

$$-i\frac{\pi}{2} \sum_{\beta''} W\left(v^-_{\beta''}, v^+_{\beta''} \right) \delta_{\beta''\beta} \mathcal{D}^-_{\beta'' m} = 2 \sum_{\beta''} \int_0^{\overline{\eta}} \frac{F^+_{\beta''\beta}(\eta)}{\sqrt{\eta}} d_{\beta'' m}(\eta) d\eta, \tag{38}$$

Considering $W\left(v^-_{\beta''}, v^+_{\beta''} \right) = 4i/\pi$ [easily proved with the aid of Eq. (11)], and $d_{\beta'' m}(\eta) \approx 0$ for the η values large enough, we finally have

$$\mathcal{D}^-_{\beta m} = \sum_{\beta''} \int_0^{\infty} \frac{\left[F^-_{\beta''\beta}(\eta) \right]^*}{\sqrt{\eta}} d_{\beta'' m}(\eta) d\eta = \int_0^{\infty} \left[\Psi^-_{\epsilon\beta m}(\mathbf{r}) \right]^* D\Psi_{ini}(\mathbf{r}) d\mathbf{r}. \tag{39}$$

It can be shown that the expression of the outgoing wave function (32) reduces to that for H atoms, as given in Ref.[9], if $V(r)$ reduces to the Coulomb potential.

C. Numerical integration of the coupled equations

In matrix notation, the coupled-channel Schrödinger equations (18) are written as

$$\left[I\frac{d^2}{d\eta^2} + Q(\eta)\right] F(\eta) = 0 \tag{40}$$

where matrix elements of Q are given by

$$Q_{\beta''\beta'}(\eta) = \left(\frac{1}{2}\epsilon - \frac{m^2-1}{4\eta^2} + \frac{1}{4}\mathscr{F}\eta - \frac{\beta'}{\eta}\right)\delta_{\beta''\beta'} - \mathcal{V}_{\beta''\beta'}(\eta). \tag{41}$$

In the very small vicinity near the nucleus, $\mathcal{V}$ approaches the hydrogenic-like potential, and therefore the nondiagonal terms of $\mathcal{V}$ are negligible. This property makes it convenient to construct solutions of the wave function $F(\eta)$ near the nucleus. The solutions have the power-series expansion form, as given in Ref.[9],

$$F_{\beta''\beta'}(\eta) = \delta_{\beta''\beta'}\eta^{\frac{|m|+1}{2}}\sum_0^\infty d_i^{\beta'}\eta^i, \tag{42}$$

where $d_i^{\beta'}(i = 0, 1, 2, ...)$ are the expansion coefficients of the series, given by

$$d_1 = -\frac{\beta_2 d_0}{1+m}, \tag{43}$$

$$d_2 = -\frac{\beta_2 d_1 + \frac{1}{2}\epsilon d_0}{2(2+m)}, \tag{44}$$

$$d_i = -\frac{\beta_2 d_{i-1} + \frac{1}{2}\epsilon d_{i-2} + \frac{1}{4}\mathscr{F} d_{i-3}}{i(i+m)}, \qquad (i \geq 3), \tag{45}$$

where $\beta_2 = 1 - \beta'$, all the coefficients are expressed in terms of d_0 with the above recursion relations, while d_0 is determined by matching $v(\eta)$ in the inner and outer region. We emphasize that the above expressions of d_i valid for any m are different from those given in Ref.[9] valid only for $m = 0$. Beyond the small region near the nucleus, the renormalized Numerov method of Johnson[17], which has been extended to integrate the coupled differential equations, is utilized to integrate the matrix equation (40). In the asymptotic region outside the core, we match the numerical solutions with their asymptotic forms given in Eq. (23) to extract the reaction matrix $\mathcal{R}$, and then obtain normalized numerical solutions. The solutions are finally used to calculate the dipole matrix elements $\mathcal{D}^{-1}_{\beta m}$ in Eq. (39).

D. Electron current density and differential cross sections

Electron current densities can be measured experimentally. It is convenient to introduce a dimensionless ratio of the electron current density to the photon current density, which can be computed from the outgoing wave function obtained above. Let us assume that a position-sensitive detector is placed under the atomic source in a uniform electric field, and the plane of the detector is perpendicular to the z axis. On the detector, the ratio of the electron current density to the photon current density in cylindrical coordinates (ρ, z, ϕ) reads[1,18]

$$R(\rho, z_{det}, \phi) = \frac{2\pi\omega}{c}\mathrm{Im}\left[\Psi^*(\mathbf{r})\frac{d\Psi(\mathbf{r})}{dz}\right]_{z=z_{det}} \tag{46}$$

where ω is the photon frequency, c is the speed of light, and the z_{det} represents the distance from the origin to the detector. This is in fact the differential cross section, but per unit area, rather than per unit solid angle. This ratio can be integrated over the azimuthal angle ϕ, and it is convenient to represent the result as a differential cross section per unit length in the ρ variable

$$\frac{d\sigma(\rho, z_{det})}{d\rho} = \int_0^{2\pi} R(\rho, z_{det}, \phi)\rho d\phi. \tag{47}$$

IV. STARK RESONANCES

Let us consider an electron in the Coulomb-Stark field. Its classical Hamiltonian equations of motion are separable, and the electron motion along the ξ coordinate is always finite, while that along the η coordinate depends on its emission angle at $\epsilon < 0$ (see Sec. II. D of Ref.[8]). If the emission angle is larger than the critical angle $\theta_c = 2\sin^{-1}(-\epsilon/2\mathscr{F})$, the electron goes to infinity along an *open* orbit; and on the contrary, if the emission angle is smaller than the critical angle, the electron is trapped forever by a potential barrier, moving along a *bound* orbit (see Sec. II. A of Ref.[8] for concepts of open and bound orbits). However, quantum theory tells that quantum waves can always tunnel though the potential barrier. Some bound orbits with special emission angles smaller than θ_c correspond to quantum waves being in quasibound Stark resonance states. Such orbits or Stark resonance states may be determined by the Bohr-Sommerfeld quantization condition.

A numerical method to locate the Stark resonances has been developed[8]. The special emission angles are sought by solving Hamiltonian equations of motion. The method is exact only for $m = 0$, but approximately valid for $m \neq 0$. Here we develop a different method to locate these Stark resonances by determining quantized β values, instead of seeking special emission angles. Using Eqs. (2, 3), we introduce the wave numbers with the Langer correction in the ξ and η coordinates as

$$k(\epsilon, \mathscr{F}, \beta, m; \xi) = \sqrt{-\frac{m^2}{4\xi^2} + \frac{\beta}{2} + \frac{\epsilon}{2} - \frac{\mathscr{F}}{4}\xi}, \tag{48}$$

$$k(\epsilon, \mathscr{F}, \beta, m; \eta) = \sqrt{-\frac{m^2}{4\eta^2} + \frac{1-\beta}{\eta} + \frac{\epsilon}{2} + \frac{\mathscr{F}}{4}\eta}. \tag{49}$$

The application of the Langer correction (namely the terms $1/4\xi^2$ and $1/4\eta^2$ are removed) is to bypass the difficulty of the semiclassical approximation breaking down near the origin. Based on the Bohr-Sommerfeld quantization rule, the semiclassical phase accumulations of $u(\xi)$ and $v(\eta)$ in the classically accessible regions are half-integral multiples of π.

$$\int_{\xi_1}^{\xi_2} k(\epsilon, \mathscr{F}, \beta, m; \xi) d\xi = \left(n_1 + \frac{1}{2}\right)\pi, \tag{50}$$

$$\int_{\eta_1}^{\eta_2} k(\epsilon, \mathscr{F}, \beta, m; \eta) d\eta = \left(n_2 + \frac{1}{2}\right)\pi, \tag{51}$$

where ξ_1, ξ_2 and η_1, η_2 denote classical turning points. For locations of Stark resonances, we utilize a minimization method[19], which has turned out to be successful in seeking complex trajectories[20]. Defining a function

$$\vartheta(\beta) = \int_{x_1}^{x_2} k(\epsilon, \mathscr{F}, \beta, m; x) dx - \left(n_i + \frac{1}{2}\right)\pi \tag{52}$$

where x represents ξ or η, and i of n_i is equal to 1 or 2, we find the minimum of $\vartheta(\beta)$ by an unconstrained nonlinear optimization procedure for each n_i when ϵ, $\mathscr{F}$, and m are fixed. It is supposed that the minimum of $\vartheta(\beta)$ should be zero (actually a very small value, like 10^{-8}, is taken).

If contour lines of both $n_1(\epsilon, \beta)$ and $n_2(\epsilon, \beta)$ are drawn in one figure, the intersection points of the $n_1(\epsilon, \beta)$ and $n_2(\epsilon, \beta)$ lines correspond to Stark resonance states. We call such a figure (ϵ, β) plot. A (ϵ, β) plot is shown in Fig. 1 at an electric field $\mathscr{F} = 3590$ V/cm and $m = 1$. To check the accuracy of the separation constants β and resonance positions ϵ_{res} calculated from the current minimization numerical technique, the obtained β and ϵ_{res} values of several Stark resonance states are compared with the results of the semiclassical open-orbit theory[8] and the quantum-mechanical approaches[9,21,22]. Good agreement is found for both separation constants and resonance positions.

V. RESULTS AND DISCUSSION

The coupled-channel theory described in the preceding sections is now applied to calculations of photoionization microscopy of Li atoms in an electric field. We assume that Li atoms in the ground state $1s^2 2s\ ^1S_0$ ($M = 0$) placed

in a uniform electric field are irradiated by a beam of laser light of tunable frequency. The laser is linearly polarized and its polarization may be parallel or perpendicular to the electric field, allowing the $\Delta M = 0$ or $\Delta M = \pm 1$ transitions, respectively. A model potential suggested by McMillian[23] is adopted to describe the interaction between the residual ion (Li^+) and the outer valence electron. The reliability of the model potential for the current purpose has been checked by calculating quantum defects for Li. The results are 0.4028, 0.0471, and 0.001 for $\ell = 0$, 1 and 2, respectively. These values are in good agreement with reported experimental and theoretical data[24]. For the ground state, the Coulomb potential and electron-electron interaction are much stronger than the interaction between the outer valence electron and electric field, so neglecting the electric field is a good approximation for the ground state of Li. The radial wave function for the initial state is obtained in the field-free case by solving the radial Schrödinger equation in spherical coordinates.

Let us consider the case of Li atoms irradiated by a beam of linearly polarized laser with polarization perpendicular to the electric field with field strength of 1010 V/cm. The standing-wave solutions were obtained by solving the coupled equation (40) for the final-state magnetic quantum number $M = \pm 1$, and the dipole matrix elements were calculated using the obtained wave functions. Figure 2 displays contour plots of the computed electron current distributions at four energies far away from any Stark resonance. The laser polarization is oriented along the vertical axis. All the contour plots are symmetric about the x-axis and the y-axis, and a smooth evolution of the interference patterns is observed. In the selected energy range and at this electric field value, the number of interference fringes is found to increase by one unit when energy increases by about 5 cm^{-1}. The selected images display from 3 to 6 bright fringes, corresponding to the opening of the $n_1 = 2$ to 5 channels. The computed electron current distributions (left panel) are compared to experimental images (right panel) at the same energies. The experimental results are obtained under rather challenging conditions and the spatial resolution is a sensitive issue in this kind of experiment. The combined limited spectral and spatial resolutions imply that some blurring affects the experimental images and reduces the contrast with respect to simulated images. Despite these limitations, all features observed in the experimental data are well reproduced by our simulations and the agreement is found to be excellent in the selected images (all chosen sufficiently far from resonances). The position of the fringes is particularly well reproduced while the agreement between experimental and calculated relative fringe intensities is less satisfactory. Indeed, the relative intensities of the various fringes are extremely sensitive to the input parameters and their exact description is more demanding than the precise determination of the number and position of fringes. Considering the experimental limitations in terms of resolution, however, the present agreement should be considered as optimal. More detailed experimental results, including, in particular, the influence of the resonances not shown here, will be reported in a forthcoming article.

From Eq. (18), one sees that the presence of the atomic core couples parabolic channels, and results in electron scattering among them. Our calculations show that at energies far away from resonances, the effect of the parabolic channel coupling is very small for the final continuum state with $M = \pm 1$, while much larger for the final state with $M = 0$. In other words, even within the core region, the ejected electron feels mostly a Coulomb-like potential plus an electric field for the $M = \pm 1$ case, but the ejected electron additionally feels the strong electron-electron interaction besides the Coulomb-like potential plus an electric field for the $M = 0$ case. This can be interpreted in terms of the so-called orbital penetration effect. The most important orbital penetration comes from the s partial wave, exhibiting the largest quantum defect. However, the contribution from the s partial wave is excluded for the final states with $M = \pm 1$ (note: the orbital angular momentum is not a good quantum number any more if an electric field exists). In order to investigate the influence of the atomic core on outgoing electron currents, it is useful to make a comparison of spatial distributions of ejected electron current densities or differential cross sections between H and Li atoms. For this purpose, we calculate photoionization of H and Li atoms, irradiated by a beam of linearly polarized laser with polarization parallel to the electric field. As the initial state of Li atoms is nondegenerate, for a meaningful comparison to the hydrogenic case, we adopt the pseudohydrogen model utilized by Harmin[12] and Gao *et al.*[25]. In this model, the coupling between the $2s$ and $2p$ states is ignored. Figure 3 plots differential cross sections of ejected electrons for pseudo-H and Li atoms at $\epsilon = -165.2$ cm^{-1} with strength of 1010 V/cm. This figure illustrates that the presence of the atomic core, by means of parabolic channel couplings, can significantly influence the differential cross sections of the ejected electrons, not only in their amplitudes but also in their spatial shapes.

It should be emphasized that the atomic core effects on outgoing electron currents or differential cross sections are reflected in both the initial and final states of Li atoms. Figure 3 displays their unified effects. It would be more instructive, however, to investigate their effects separately. For this purpose, we artificially removed the short-range spherically-symmetric core potential term of $\mathcal{V}(\eta)$ to solve the resulting coupled Schrödinger equations (18), and utilized the obtained wave functions to compute differential cross sections for a kind of artificial atom, which are assumed to be in the initial state of Li atom and the final state of H atom. This kind of artificial atoms will be hereafter called the *artificial* H atom. The differential cross sections of the artificial H and real Li atoms are compared in Fig. 4 at six energies away from the Stark resonances. The electric field strength is taken to be 1010 V/cm. From this figure, it can clearly be seen that for this specific example, the presence of the atomic core can increase the differential cross sections by a factor of 3.5 to 7.5, by means of mixing of the parabolic channels of the final state.

Contrary to what is observed in Fig. 3, however, the change of the shapes of the spatial distributions is not very remarkable. The number of interference fringes and the tendency of the smooth evolution of the interference patterns with energy remain unchanged, although the differential cross sections are shifted from the outer region to the inner regions due to parabolic channel couplings.

Let us now analyze resonance tunneling in the presence of atomic cores. For this purpose, assume that Li atoms in the ground state are irradiated by the π-polarized laser light and excited to Rydberg states at some hydrogenic resonance positions of H atoms. To seek a resonance, it is convenient to utilize the (ϵ, β) plot, as suggested in Sec. IV. For Stark H atoms, two resonances (n_1,n_2,m) = $(10, 18, 0)$ and $(17, 12, 0)$ were found to be at -152.168 and -119.503 cm^{-1}. These values are in good agreement with the quantum-mechanical results, -152.2031 and -119.5349 cm^{-1}. The differential cross sections calculated using the corresponding outgoing wave functions of ejected electrons for Li and artificial H atoms are drawn in Fig. 5. The difference between the differential cross sections of Li and artificial H atoms is very pronounced, not only in their amplitudes, but also in their shapes (see the upper panel of each plot).

When, however, the contributions from the resonances are removed from the hydrogenic differential cross sections, the spatial distributions are found to be very similar, as displayed in the lower panels of Fig. 5 where there are the differences only in their amplitudes. It should be emphasized that for Li atoms, the contribution from the parabolic partial waves, with the same n_1 as in the $(10, 18, 0)$ and $(17, 12, 0)$ resonances of H atoms, are also removed for comparison. Furthermore, for each energy, one sees that the cyan (light gray) curves in the upper and lower panel are very close. That means that these two energy locations do not correspond to Li resonances, and the contributions from the parabolic partial waves with $n_1 = 10$ or 17 to the Li differential cross sections are insignificant. This is physically reasonable, because the resonance conditions holding for a pure Coulomb plus electric field situation do not apply anymore, and as a consequence, no resonance tunneling is observable. For multielectron atoms, the condition to produce resonance tunneling may be restored if the energy is shifted by a small amount. Thus one may expect that resonances in multielectron atoms are very close to resonances in H atoms. Such an expectation was earlier confirmed by experiment[12]. The photoionization spectrum of Na atoms shows that the differences between the Stark resonances in Na and H atoms are extremely small (see Fig. 8 of Ref.[12] where resonance locations of H atoms, accompanying each of Li resonances, are labeled).

The above analysis tells that one may search for Li resonances near resonance locations of H atoms by monitoring differential cross sections. At -152.2897 cm^{-1}, i.e. 0.0866 cm^{-1} just below the Stark resonance $(10, 18, 0)$ of H, a Li resonance has been found. The computed differential cross sections of Li atoms and artificial H atoms at this energy are compared in Fig. 6. A significant difference is clearly seen in the amplitudes of the distributions, but the shapes of the distributions, including the number and positions of the fringes (each peak corresponds to one interference fringe on the detector), are very similar. Contrary to the above situation, no resonance was found for Li in the energy region near the $(17, 12, 0)$ resonance in H, given in the light part of Fig. 5. This is not surprising. One may not expect that the condition to produce the resonance tunneling for multielectron atoms is always satisfied at any Stark resonance of H atoms. For example, an experimental photoionization spectrum of Na atoms in an electric field of $\mathscr{F} = 3590$ V/cm does not explicitly display any resonance near the (24,0,1) resonance in H atoms (see Fig. 8 of Ref.[12]). It appears that this resonance is too small to be observable.

In order to observe the influence of the atomic core on resonance tunneling for the $M = 1$ case, let us assume that ground-state Li and artificial H atoms, placed in an electric field of 1010 V/, are irradiated by the σ^+ laser light and excited to Rydberg states at some hydrogenic resonance positions of H atoms. We sought a Li resonance at -150.2556 cm^{-1}, very close to the resonance $(10, 18, 1)$ in H at -150.2451 cm^{-1}. The differential cross sections for Li and artificial H atoms at the Li resonance location are drawn in Fig. 6. They obviously differ solely in the magnitudes while their shapes are practically identical. By comparing the $M = 0$ and $M = 1$ cases, corresponding to the left and right parts of Fig. 6 respectively, we conclude that when the core penetration is important, one observes changes in both the amplitude and the shape of differential cross sections, while only the amplitude is affected for the weak penetration. Overall, depending on the ejected electron energy, the electric field strength and the azimuthal quantum number, the atomic core remarkably influences the amplitudes of differential cross sections, and may change the shapes of the distributions with respect to the hydrogenic situation. This qualitative conclusion is supported by all the examples given in Figs. 3–6 and can be quantitatively traced by comparing the results with and without nondiagonal terms of the potential $\mathcal{V}(\eta)$.

VI. CONCLUSION

A quantum-mechanical coupled-channel theory has been developed to simulate spatial distributions of electron current densities and differential cross sections, produced in photoionization for nonhydrogenic atoms in the presence of a uniform external electric field. The outgoing electron wave function has been derived in the representation of coupled channels, and the coupled Schrödinger equations have been solved using the renormalized Numerov method.

This theory, which can be regarded as an extension of our earlier work devoted to hydrogenic atoms in a uniform electric field[9], has been applied to photoionization of ground-state Li atoms and computed spatial distributions of electron current densities were found to be in good agreement with the corresponding experimental images. A thorough investigation concerning the influence of atomic cores on differential cross sections has shown that the atomic core alters significantly the differential cross sections for Li atoms with respect to the corresponding hydrogenic distributions. The effect was also found to be even more pronounced under quantum resonant tunneling situations, particularly when the penetration of the outer electron into the core becomes significant.

Acknowledgments

This work was supported by the National Science Foundation under Grant No. PHY-0969381 and by the Marie Curie International Incoming Fellowship (FP7-PEOPLE-2009-IIF-252714).

[1] I. I. Fabrikant, JETP **52**, 1045 (1980).
[2] Yu. N. Demkov, V. D. Kondratovich, and V. N. Ostrovsky, JETP Lett. **34**, 403 (1981).
[3] C. Nicole, I. Sluimer, F. Rosca-Pruna, M. Warntjes, M. J. J. Vrakking, C. Bordas, F. Texier, and F. Robicheaux, Phys. Rev. Lett. **85**, 4024 (2000).
[4] C. Nicole, H. L. Offerhaus, M. J. J. Vrakking, F. Lépine, and C. Bordas, Phys. Rev. Lett. **88**, 133001 (2002).
[5] F. Lépine, S. Zamith, A. de Snaijer, C. Bordas, and M. J. J.Vrakking, Phys. Rev. Lett. **93**, 233003 (2004).
[6] C. Bordas, F. Lépine, C. Nicole, and M. J. J. Vrakking, Phys. Rev. A **68**, 012709 (2003).
[7] F. Lépine, C. Bordas, C. Nicole, and M. J. J. Vrakking, Phys. Rev. A **70**, 033417 (2004).
[8] L. B. Zhao and J. B. Delos, Phys. Rev. A **81**, 053417 (2010).
[9] L. B. Zhao and J. B. Delos, Phys. Rev. A **81**, 053418 (2010).
[10] F. Robicheaux and J. Shaw, Phys. Rev. A **56**, 278 (1997).
[11] D. A. Harmin, Phys. Rev. A **24**, 2491 (1981).
[12] D. A. Harmin, Phys. Rev. A **26**, 2656 (1982).
[13] F. Texier, Phys. Rev. A **71**, 013403 (2005).
[14] B. R. Johnson, J. Chem. Phys. **67**, 4086 (1977).
[15] W. E. Milne, Phys. Rev. **35**, 863 (1930).
[16] M. G. J. Fink and P. Zoller, Phys. Rev. A **39**, 2933 (1989).
[17] B. R. Johnson, J. Chem. Phys. **69**, 4678 (1978).
[18] I. I. Fabrikant, J. Phys. B, **23**, 1139 (1990).
[19] M. Abramowitz and I. E. Stegun, *Handbook of Mathematical Functions* (Department of Commerce, Washington, DC, 1972).
[20] I. I. Fabrikant and G. A. Gallup, Phys. Rev. A **79**, 013406 (2009).
[21] A. Alijah and A. von Hopffgarten, J. Phys. B, **27**, 843 (1994).
[22] G. Alvarez, R. J. Damburg and H. J. Silverstone, Phys. Rev. A **44**, 3060 (1991).
[23] W. L. McMillian, Phys. Rev. A **4**, 69 (1971).
[24] G. L. Snitchler and D. K. Watson, J. Phys. B, **19**, 259 (1986).
[25] J. Gao, J. B. Delos, and M. Baruch, Phys. Rev. A **46**, 1449 (1992); J. Gao and J. B. Delos, Phys. Rev. A **46**, 1455 (1992).

TABLE I: Comparison of separation constants β and resonance positions ϵ_{res} (in cm^{-1}) for Stark H atoms between the current and other calculations at $\mathscr{F} = 5714$ V/cm.

	β		ϵ_{res}				
(n_1, n_2, m)	MNT[a]	FQM[b]	MNT[a]	FQM[b]	Ref.[8]	Ref.[21]	Ref.[22]
(22,0,0)	0.99101	0.99153	-46.406	-46.679	-46.406	-46.925	-46.53
(21,0,0)	0.98743	0.98772	-76.798	-76.954	-76.798	-77.176	-76.77
(20,1,0)	0.96138	0.96188	-95.733	-96.029	-95.733	-96.196	-95.87
(19,1,0)	0.95264	0.95285	-127.377	-127.492	-127.377	-127.647	-127.31
(18,2,0)	0.91922	0.91951	-144.625	-144.806	-144.625	-144.915	-144.64
(17,3,0)	0.88438	0.88481	-162.059	-162.355	-162.059	-162.413	-162.21
(20,0,1)	0.97431	0.97471	-86.096	-86.315			-86.14
(19,1,1)	0.94789	0.94820	-105.404	-105.582			-105.48
(18,1,1)	0.93598	0.93621	-135.923	-136.062			-135.89
(17,2,1)	0.90184	0.90219	-153.249	-153.486			-153.33
(16,3,1)	0.86636	0.86677	-170.839	-171.135			-171.02
(15,3,1)	0.84612	0.84628	-202.429	-202.538			-202.37

[a] MNT: the minimization numerical technique.
[b] FQM: the fully quantum-mechanical approach of Ref.[9].

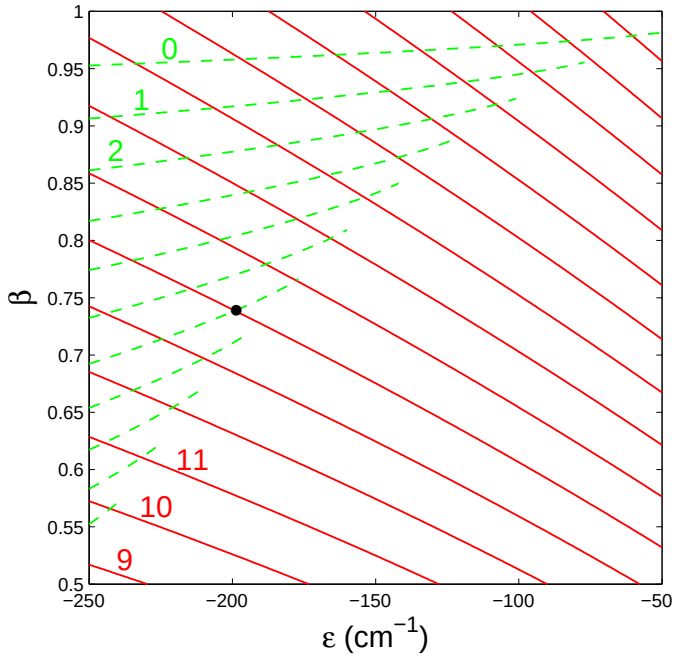

FIG. 1: (Color online) The (ϵ, β) plot of Stark H atoms at $\mathscr{F} = 3590$ V/cm and $m = 1$. The contour lines are $n_1 = 9, 10, ..., 23$ (solid from bottom to top) and $n_2 = 0, 1, ..., 10$ (dashed from top to bottom), respectively. Any one of the intersection points of the n_1 and n_2 lines corresponds to a Stark resonance state, specified by (n_1, n_2, m). The black dot located at $\epsilon = -199.1506$ cm^{-1} is the intersection of $n_1 = 14$ and $n_2 = 6$. It corresponds to the (14, 6, 1) resonance.

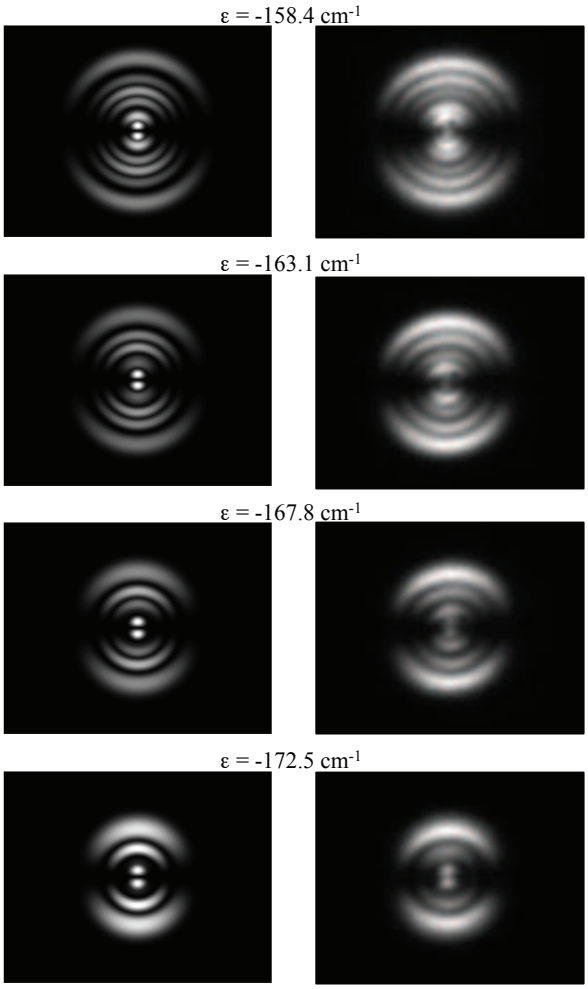

FIG. 2: Comparison of theoretical (left panel) and experimental (right panel) ejected electron currents of Li atoms at four energies away from Stark resonances. The electron currents are produced due to photoionization of ground-state Li atoms in an electric field along the z axis with field strength $\mathscr{F} = 1010$ V/cm. The Li atoms are irradiated by a linearly polarized laser light with polarization direction perpendicular to the electric field. The detector is located at $z_{det} = -1000$ μm. Note evolution of the interference patterns with energies.

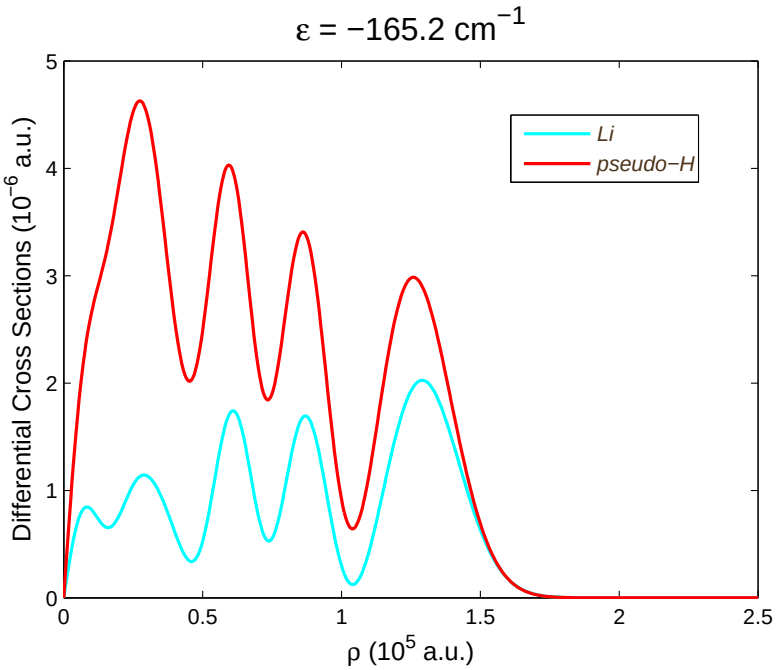

FIG. 3: (Color online) Differential cross sections for pseudo-H (red or dark gray) and Li (cyan or light gray) atoms, placed in an electric field $\mathscr{F} = 1010$ V/cm, at energy $\epsilon = -165.2$ cm^{-1}. The Li and pseudo-H atoms are irradiated by a linearly polarized laser light with polarization direction parallel to the electric field ($M = 0$). The Li atoms are initially in the ground state and for comparison purpose, the initial state of H atoms is assumed to be the metastable $2s$ state, *i.e.* a pseudohydrogen model is adopted (strictly speaking, there is mixing between $2s$ and $2p$, see Ref.[9] for details). The difference of the differential cross sections between Li and pseudo-H atoms illustrates the atomic core effect.

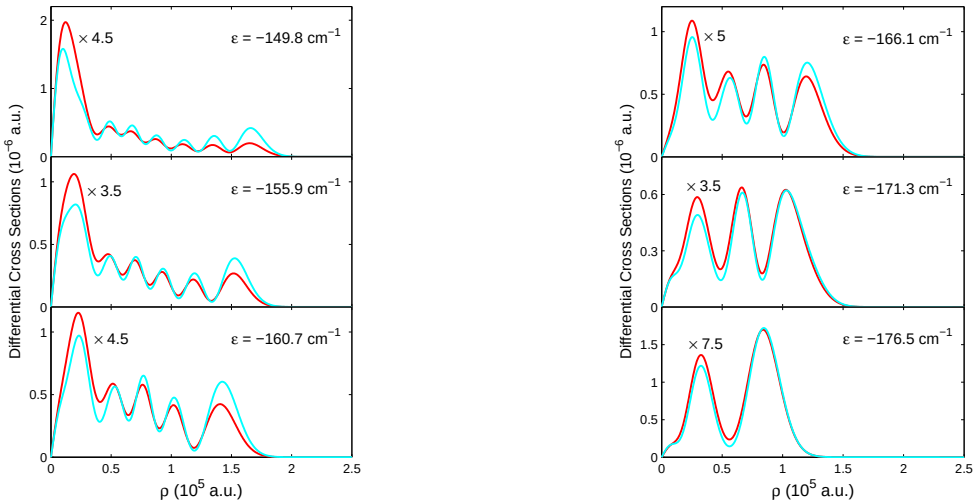

FIG. 4: (Color online) Differential cross sections of the ejected electrons, produced due to photoionization of ground-state Li atoms in an electric field $\mathscr{F} = 1010$ V/cm. The laser light is linearly polarized with polarization direction parallel to the electric field. The electron energies range from -176.5 to -149.8 cm^{-1} away from Stark resonances. The cyan (light gray) and red (dark gray) curves represent the differential cross sections for Li and *artificial* H atoms, respectively. In the latter case, hydrogenic wave functions for the final states are utilized. The comparison displays the influence of atomic cores on the differential cross sections or the ejected electron currents. Note that the red (dark gray) curves are multiplied by a factor of 3.5 to 7.5.

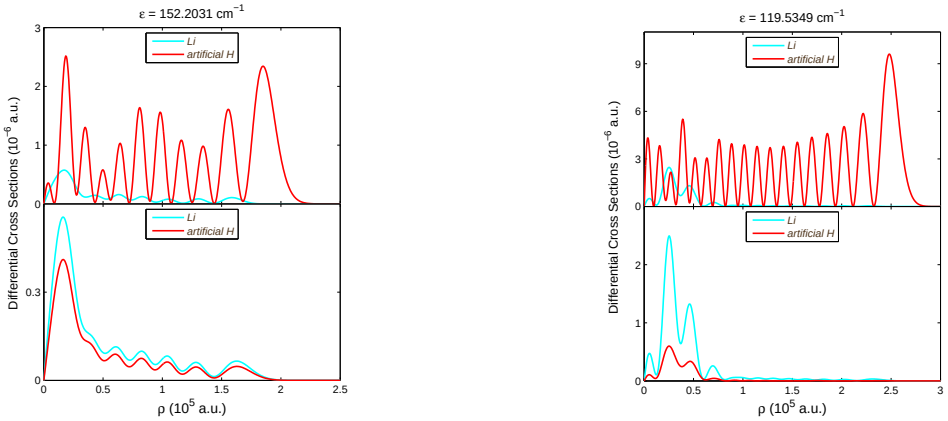

FIG. 5: (Color online) The same as Fig. 4, but at energies -152.2031 and -119.5349 cm^{-1}, corresponding to two resonances $(10, 18, 0)$ and $(17, 12, 0)$ in H atoms, respectively. The cyan (light gray) and red (dark gray) curves represent differential cross sections for Li and artificial H atoms, respectively. The curves in the lower panels are the same as in the corresponding upper panels but the contribution from the resonance state $(10, 18, 0)$ or $(17, 12, 0)$ for H, and the contribution from the parabolic partial wave with $n_1 = 10$ or 17 for Li, are removed. The comparison illustrates the influence of atomic cores on quantum resonance tunneling.

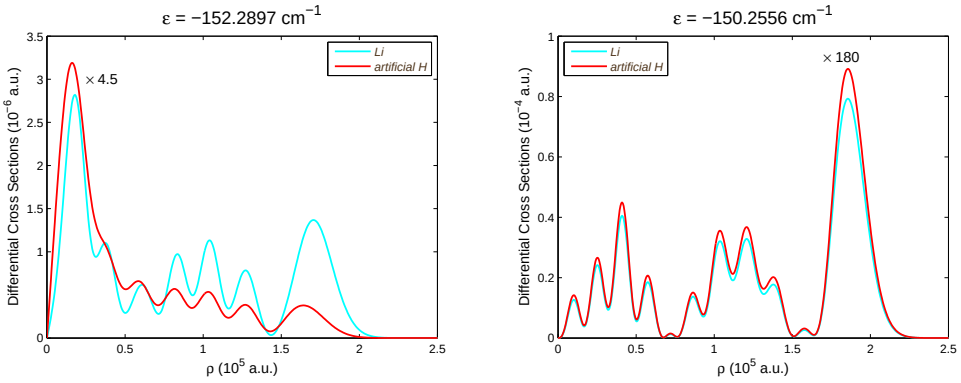

FIG. 6: (Color online) Comparison of differential cross sections for Li and artificial H atoms at Stark resonance locations of Li atoms. The two resonances for Li atoms are very close to two resonances $(10, 18, 0)$ and $(10, 18, 1)$ for H atoms, respectively, at -152.2031 and -150.2451 cm^{-1}. The cyan (light gray) and red (dark gray) curves represent differential cross sections for Li and artificial H atoms, respectively.